Spectral and Polarization Vision:
Spectro-polarimetric Real-world Dataset

Yujin Jeon[1],[*]   Eunsue Choi[1],[*]   Youngchan Kim[1]   Yunseong Moon[1]
Khalid Omer[2]   Felix Heide[3]   Seung-Hwan Baek[1]

[1] POSTECH   [2] Meta   [3] Princeton University

Abstract

Image datasets are essential not only in validating existing methods in computer vision but also in developing new methods. Most existing image datasets focus on trichromatic intensity images to mimic human vision. However, polarization and spectrum, the wave properties of light that animals in harsh environments and with limited brain capacity often rely on, remain underrepresented in existing datasets. Although spectro-polarimetric datasets exist, these datasets have insufficient object diversity, limited illumination conditions, linear-only polarization data, and inadequate image count. Here, we introduce two spectro-polarimetric datasets: trichromatic Stokes images and hyperspectral Stokes images. These novel datasets encompass both linear and circular polarization; they introduce multiple spectral channels; and they feature a broad selection of real-world scenes. With our dataset in hand, we analyze the spectro-polarimetric image statistics, develop efficient representations of such high-dimensional data, and evaluate spectral dependency of shape-from-polarization methods. As such, the proposed dataset promises a foundation for data-driven spectro-polarimetric imaging and vision research. Dataset and code will be publicly available.

1. Introduction

Recent progress in computer vision can be largely attributed to comprehensive studies of real-world image datasets, such as ImageNet [14]. Foundation models [1, 35, 53, 64] further underscore data significance. Most of these datasets comprise trichromatic intensity images, inspired by human visual perception, enabling machines to emulate human vision with trichromatic RGB cameras. As such, the datasets have facilitated the development of low-cost, camera-based autonomous agents capable of perceiving and interacting with our world, as we do. However, the reliance on trichro-

matic intensity in existing image datasets also comes with inherent limitations for analyzing objects in depth. Examples include textureless surface, low-albedo objects, and transparent materials.

Light possesses wave properties, including polarization and spectrum [9], which are not faithfully captured by trichromatic intensity imaging. While these properties are invisible to human, animals like honeybees and ants leverage the polarization and spectrum for navigation and other tasks. Horvath and Varju [25] provide diverse examples and mechanisms of spectral and polarimetric vision in animals. Partly drawing inspiration from nature, researchers have extended the analysis of spectrum and polarization to a variety of fields, including computer vision, robotics, and astronomy. This has spurred interest in polarimetric [7, 8, 38, 49] and hyperspectral imaging [2, 10, 28], and more recently, their integration into spectro-polarimetric imaging [3, 17, 18, 23, 26, 45, 47, 50, 54, 67]. Prior work using spectro-polarimetric images has shown potential for skin analysis [67], vegetation classification [63], shape reconstruction [27], object recognition [13], and segmentation [30, 55].

There are existing spectro-polarimetric datasets, summarized in Figure 2, that have been invaluable for these analysis [19, 38, 39, 52] and training neural networks [4, 11, 22, 36, 40–42, 46, 48]. However, these datasets unfortunately do not capture the diversity of real-world spectro-polarimetric images as effectively as their trichromatic intensity counterparts do. They typically suffer from limited object, scene, and illumination diversity, contain primarily linear polarization information, and offer a small number of images. To advance the field, we propose a comprehensive spectro-polarimetric dataset that encompasses: (1) *Full Stokes polarimetric data*, including both linear and circular polarization states, represented by Stokes vectors [9] for each pixel and wavelength. (2) *A diverse range of spectral channels*, facilitating in-depth exploration of the interplay between spectrum and polarization. (3) *A broad array of real-world scenes*, crucial for extracting meaningful statis-

---

tics and relationships within spectro-polarimetric images.

To this end, we introduce two novel spectro-polarimetric datasets designed to cover real-world spectro-polarimetric scenes: a trichromatic Stokes dataset consisting of 2,022 images, and a hyperspectral Stokes dataset containing 311 images across 21 spectral channels. The trichromatic Stokes dataset covers a wider range of scenes thanks to its convenient capture setup and process. The hyperspectral Stokes dataset provides richer spectral-polarimetric information than the trichromatic Stokes dataset. Both datasets cover a variety of natural indoor and outdoor scenes. Each image in these datasets is annotated with four specific parameters: the type of environment (indoor or outdoor), the illumination conditions (clear/cloudy sunlight or white/yellow office light), the timestamp of capture, and the scene categorization (either object- or scene-oriented).

Utilizing these datasets, we systematically analyze the statistics of real-world spectro-polarimetric images. We focus on examining statistics of Stokes vectors, in addition to the gradients and polarimetric attributes associated with them. We also conduct an analysis of unpolarized and polarized images derived through polarimetric decomposition. We then develop two efficient spatio-spectral-polarimetric representations using principal component analysis (PCA) and implicit neural representation (INR). These representations exhibit effective denoising capabilities and low memory footprints by exploiting the compressible structure of spectro-polarimetric images. We also analyze the impact of intensity denoising for spectro-polarimetric images, spectral dependency of shape-from-polarization methods, and environment dependency on the statistics of spectro-polarimetric images.

In summary, we make the following contributions.

- We introduce a trichromatic Stokes dataset and a hyperspectral Stokes dataset, featuring 2,333 diverse annotated indoor and outdoor scenes under various illumination conditions, which encompasses full-Stokes polarization data for linear and circular states.
- We develop efficient spatio-spectral-polarimetric representations and analyze real-world spectro-polarimetric images, encompassing Stokes vectors and their gradients, unpolarized and polarized images, shape from polarization, denoising, and environment dependency.

2. Related Work

Spectro-polarimetric Image Dataset Several datasets have been introduced for analyzing polarization and spectral information. With the advent of trichromatic linear-polarization cameras, a line of work has attempted to acquire trichromatic linear-polarization images, ranging from a few objects and scenes [5, 11, 42, 52] to a large number of scenes for specific target applications such as reflection separation [40, 46] and glass segmentation [48].
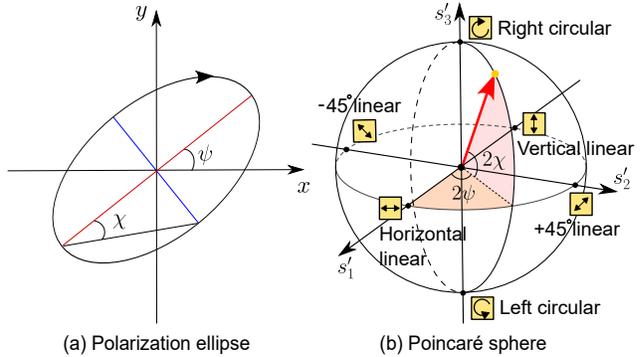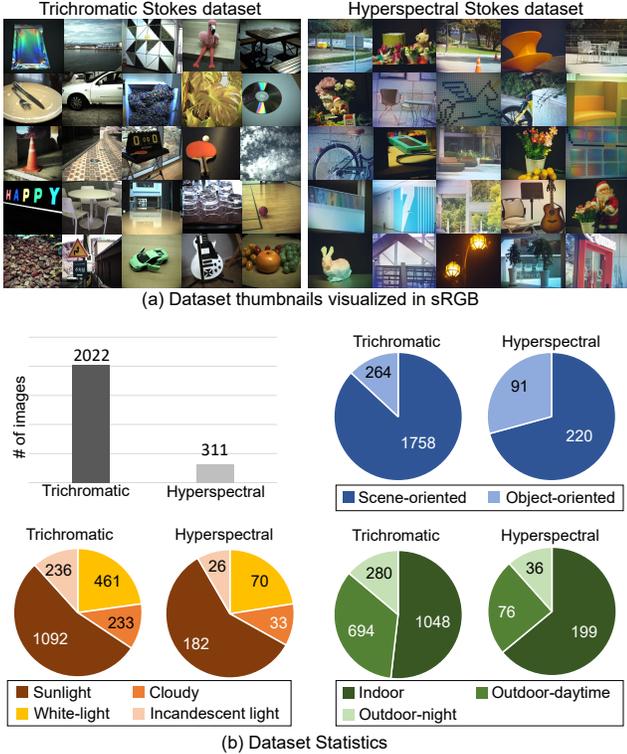

Figure 1. **Two representative polarization visualizations.** (a) Polarization ellipse depicts the electric-field oscillation projected onto a plane tangent to the light propagation. (b) Poincaré sphere visualizes the polarization state of light on the normalized Stokes-vector axes s_1', s_2', s_3'.

Lapray et al. [39] acquire linear-polarization images for the near-infrared spectral band, albeit only on 10 objects. Fan et al. [19] acquire the first multispectral full-Stokes polarimetric dataset covering linear and circular states, while it only contains 64 flat objects captured in a lab environment. Our proposed datasets enables analyzing the statistics of real-world spectro-polarimetric images, which cannot be achieved by prior datasets. See Figure 2 for a comprehensive comparison.

Applications of Spectro-polarimetric Imaging Spectro-polarimetric information has been investigated for diverse vision and imaging tasks. Using linear-polarization images has found applications in shape reconstruction [4, 5, 7, 16, 21, 31, 41, 70], appearance acquisition [15, 36], removing reflections [37, 40, 46, 51, 59, 62], transparent-object segmentation [33, 48], seeing through scattering [20, 43, 68], and image enhancement [69]. Trichromatic Stokes images have been used for tone-mapping [12] and seeing through scattering [6]. Expanding into multi-spectral domain, spectral-polarimetric analysis has been applied to object recognition [13], skin analysis [67], dehazing [61], specular reflection inpainting [29], background segmentation [30] and tensor representation [65]. In addition to vision tasks, spectro-polarimetric imaging has been used for various biological applications, such as marsh vegetation classification [63], coastal wetland classification [55] and leaf nitrogen determination [44]. While the aforementioned studies demonstrate the benefits of using spectro-polarimetric data, we believe that the full potential of spectro-polarimetric images is still locked by the absence of real-world spectro-polarimetric datasets.

3. Background on Polarization

Polarization, the oscillation pattern of the electric field, can be represented using a Stokes vector, $\mathbf{s} = [s_0, s_1, s_2, s_3]^{\mathsf{T}}$.

Trichromatic Stokes dataset   Hyperspectral Stokes dataset

(a) Dataset thumbnails visualized in sRGB

(b) Dataset Statistics

Dataset	Polar.	# of bands	Scene count	Scene diversity
[41]	LP	1	522	Outdoor scenes
[5]	LP	1	300	Indoor objs.
[39]	LP	6	10	Indoor objs.
[52]	LP	3	40	Indoor objs.
[11]	LP	3	3	Indoor multiview
[11]	LP	3	2	Synthetic multiview
[22]	LP	3	6	Indoor multiview
[40]	LP	3	807	Reflective objs.
[42]	LP	3	500	Outdoor scenes
[36]	LP	3	44,300	Synthetic
[46]	LP	3	3,200	Reflective objs.
[48]	LP	3	4,500	Transparent objs.
[38]	LP	3	2,000	Indoor/outdoor scenes
[19]	LP, CP	18	67	Flat objs.
[34]	LP, CP	21	4	Synthetic multiview
[34]	LP, CP	21	4	Indoor/outdoor multiview
Ours (RGB)	LP, CP	3	2022	Indoor/outdoor scenes
Ours (HS)	LP, CP	21	311	Indoor/outdoor scenes

Figure 2. **Spectro-polarimetric image datasets.** We present trichromatic and hyperspectral Stokes datasets of which thumbnails are shown in (a) and label statistics in (b). The table shown on the right compares our datasets with existing spectro-polarimetric datasets. Ours are the only datasets that encompass both linear (LP) and circular (CP) polarization over multiple of spectral bands for diverse real scenes.

s_0 denotes the total intensity, s_1 and s_2 describe the differences in the intensity of linearly-polarized components at orientations of $0°/90°$ and $45°/-45°$, respectively. s_3 is the difference in intensity between right- and left-circularly polarized components.

Figure 1 shows two visualization methods for polarization, the polarization ellipse and Poincaré sphere. Polarization ellipse can be described in terms of the orientation angle ψ and ellipticity χ with respect to the projected Stokes vector x and y axes [9]. The Poincaré sphere visualizes polarization in a three-dimensional space, using the normalized Stokes-vector elements relative to the total intensity: $s_1' = s_1/s_0$, $s_2' = s_2/s_0$, $s_3' = s_3/s_0$. To effectively analyze a Stokes vector, one can compute the degree of polarization (DoP) denoted as ρ, the angle of linear polarization (AoLP) represented by ψ, and the ellipticity angle given by χ, that is

$$\rho = \frac{P}{s_0}, \ \psi = \frac{1}{2}\arctan\left(\frac{s_2}{s_1}\right), \ \chi = \frac{1}{2}\arctan\left(\frac{s_3}{L}\right), \ (1)$$

where $P = \sqrt{s_1^2 + s_2^2 + s_3^2}$ and $L = \sqrt{s_1^2 + s_2^2}$.

We also use the polarimetric visualization method proposed by Wilkie et al. [60] using DoP, AoLP, and chirality of polarization (CoP). CoP describes the left- or right-handedness of the circularly polarized component, which is

related to χ. Finally, the Mueller matrix $\mathbf{M} \in \mathbb{R}^{4\times4}$ describes the change of a Stokes vector: $\mathbf{s}_{\text{out}} = \mathbf{M}\mathbf{s}_{\text{in}}$, where $\mathbf{s}_{\text{in}}$ and $\mathbf{s}_{\text{out}}$ are the input/output Stokes vectors. For more details on polarization, we refer to the book by Collett [9].

4. Spectro-polarimetric Dataset

We introduce a trichromatic Stokes dataset comprising 2022 Stokes images and a hyperspectral Stokes dataset with 311 Stokes images at 21 spectral channels. Both datasets cover natural real-world indoor and outdoor scenes. Each Stokes image is accompanied by four labels detailing: (1) the environment (indoor or outdoor), (2) the illumination condition, including clear or cloudy sunlight and white or incandescent light, (3) the time of image capture, (4) the scene type, distinguishing between object-oriented and scene-oriented. Figure 2 shows thumbnails, label statistics, and comparison of our datasets to existing ones. Prior datasets suffer from a narrow range of scenes, restricted illumination conditions, linear polarization only, and fewer images.

Acquisition We acquire the datasets using two imaging systems depicted in Figure 3(a), proposed and developed by previous studies [34, 56]. First, the trichromatic Stokes camera by Tu et al. [56] incorporates on-sensor quarter-wave plates (QWPs) and linear polarizers (LPs) [9]. This al-
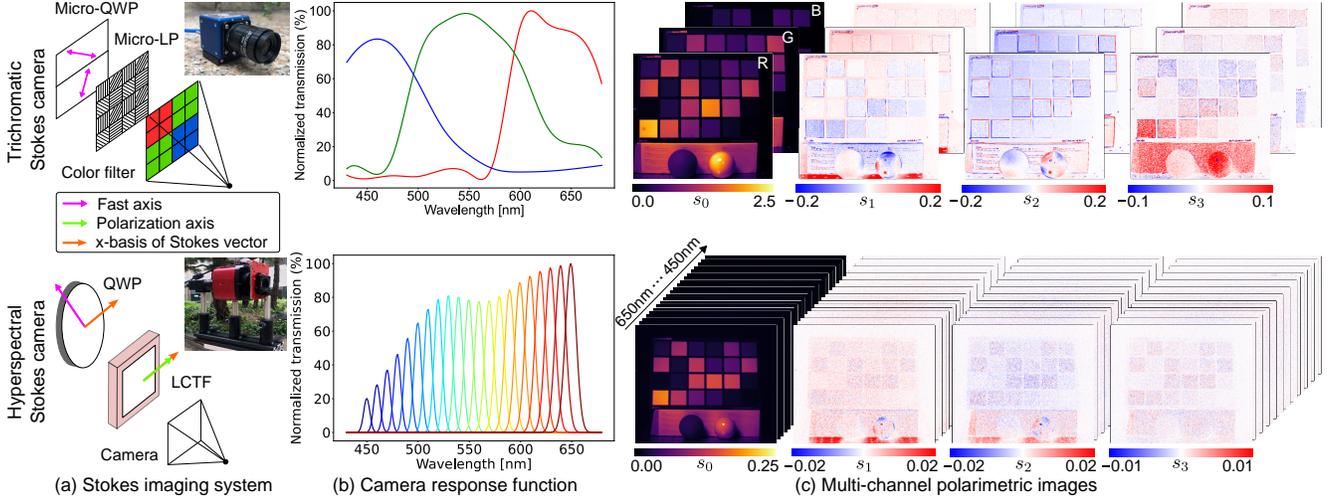
3

Figure 3. **Acquisition of spectro-polarimetric images.** We capture spectro-polarimetric images using (a) trichromatic and hyperspectral Stokes cameras [34, 57]. (b) Camera response functions. (c) Reconstructed raw Stokes images per each spectral channel.

lows for single-shot capture of trichromatic Stokes images, enabling convenient data collection on diverse scenes. The resolution of a trichromatic Stokes image is 2100 (width) × 1920 (height) × 3 (RGB) × 4 (Stokes elements). Second, the hyperspectral Stokes camera from Kim et al. [34] captures images by sequentially scanning 21 spectral channels from 450 nm to 650 nm in 10 nm increments with a LCTF which functions as a LP. For each spectral channel, we capture images by rotating a QWP with a fixed LP. This system enables a detailed analysis of the interplay between wavelength and polarization. The resolution of a hyperspectral Stokes image is 612 (width) × 512 (height) × 21 (wavelengths) × 4 (Stokes elements).

Spectro-polarimetric Image Formation Using the two imaging systems, we capture raw images from which a per-pixel Stokes vector for each spectral channel is reconstructed. We introduce an unified image formation model that can be applied to both cameras. Suppose a light ray with a Stokes vector $\mathbf{s}_\lambda$ at wavelength λ impinges on a Stokes camera. As the light passes through polarization-modulating optical filters modeled by the Mueller matrix $\mathbf{M}(\Theta)$, its Stokes vector transforms. Θ denotes the polarization-filter configuration. The camera sensor then captures light intensity, represented by the first element of the Stokes vector. The recorded intensity, $I_c(\Theta)$, at a spectral channel c and polarimetric filter configuration Θ, is described by

$$
\begin{aligned}
I_c(\Theta) &= \left[\int \Omega_{c,\lambda} \mathbf{M}_c(\Theta) \mathbf{s}_\lambda d\lambda \right]_0 \\
&= \left[\mathbf{M}_c(\Theta) \int \Omega_{c,\lambda} \mathbf{s}_\lambda d\lambda \right]_0 \\
&= \left[\mathbf{M}_c(\Theta) \mathbf{s}_c \right]_0 ,
\end{aligned}
\tag{2}
$$

where $\Omega_{c,\lambda}$ is the spectral transmission per channel at wavelength λ shown in Figure 3(b). $[x]_0$ denotes the first-element of the Stokes vector x, which is the total intensity. For a spectral channel c, $\mathbf{M}_c$ is the Mueller matrix of the polarization-modulating optics, and $\mathbf{s}_c$ is the Stokes vector.

For polarization modulation, both cameras utilize a QWP and a LP, yielding the Mueller matrix

$$
\mathbf{M}_c(\Theta) = \mathbf{C}_c \mathbf{Q}_c(\theta_1) \mathbf{P}_c(\theta_2),
\tag{3}
$$

where $\mathbf{C}_c$ is the error-compensating calibration matrix [34, 57]. $\mathbf{Q}_c$ and $\mathbf{P}_c$ are the QWP and LP Mueller matrices [9], respectively. The set $\Theta = \{\theta_1, \theta_2\}$ denotes the corresponding angles of the QWP fast axis and the LP polarization axis, which is set for accurate Stokes vector reconstruction [34, 57]. Lastly, we determine the per-channel Stokes vector $\mathbf{s}_c$ by solving the least-squares problem

$$
\underset{\mathbf{s}_c}{\operatorname{argmin}} \sum_{i=1}^{|\Theta|} \left(I_c(\Theta_i) - [\mathbf{M}(\Theta_i)\mathbf{s}_c]_0 \right)^2 .
\tag{4}
$$

For the hyperspectral Stokes camera, we use four configurations with the rotating QWP. For the trichromatic Stokes camera, the fixed micro-filter setup shown in Figure 3(a) gives four/eight configurations for the (red, blue) channels and the green channel, respectively.

Figure 3(c) shows the reconstructed Stokes images. A Stokes vector is physically-valid if DoP meets the following inequality: $0 \leq \rho \leq 1$. 99% of the reconstructed Stokes vectors in our datasets satisfy the DoP condition. For the following dataset analysis, we filter out Stokes vectors violating the DoP condition and the unstable Stokes vectors reconstructed from saturated and underexposed pixel intensity values.

4

(a) Top 40 PCA bases of hyperspectral Stokes vector components

(b) Qualitative results (DoP/AoLP)

(c) Proportion of variance (log scale)

(d) BPP and MSE of PCA

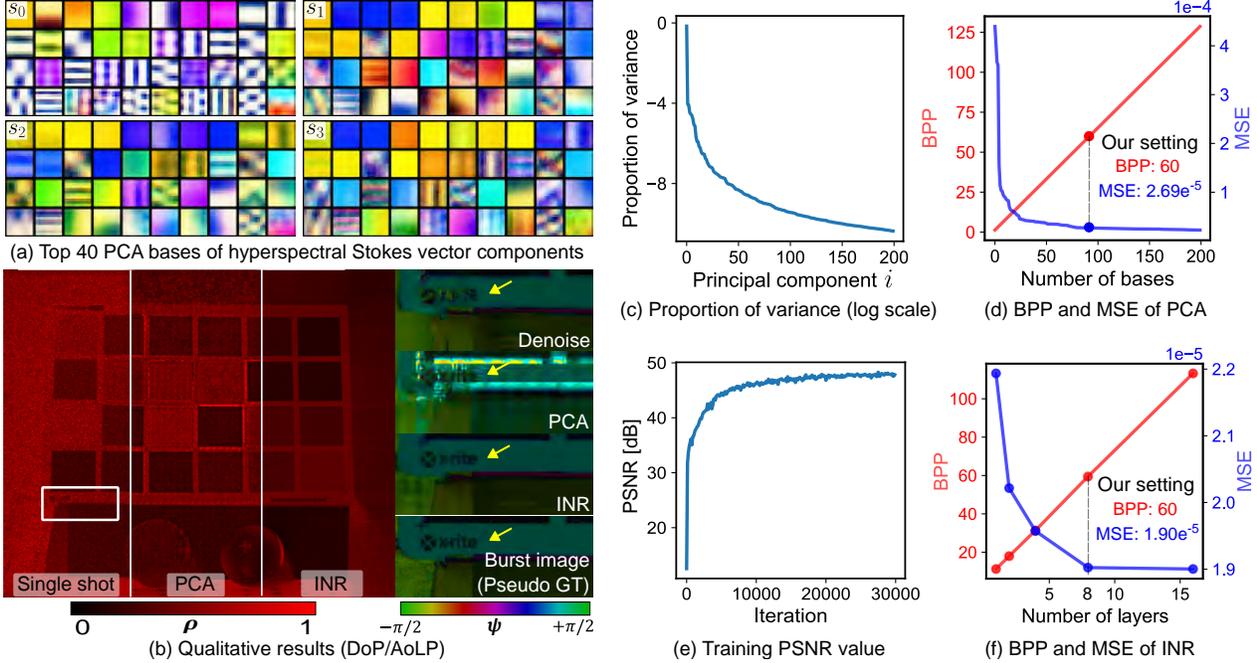(e) Training PSNR value

(f) BPP and MSE of INR

Figure 4. **Efficient spatio-spectral-polarimetric representations.** (a) PCA basis of the hyperspectral Stokes dataset in sRGB. (b) Qualitative results of PCA and INR compared to single-shot denoising [66] at 550 nm. (c) Proportion of variance with respect to each PCA basis in order, $\log(\sigma_i^2 / \sum_n \sigma_n^2)$, where σ_i denotes standard deviation of the i-th basis. (d) BPP and MSE analysis of PCA with respect to the number of PCA bases. (e) Training PSNR curve of INR. (f) BPP and MSE value of INR with respect to the number of MLP layers.
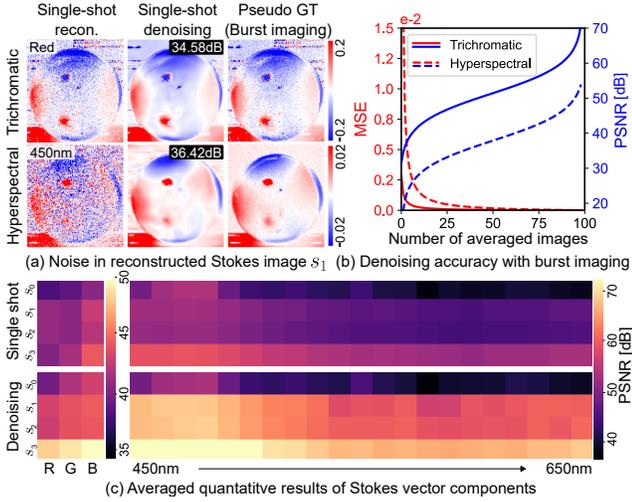

(a) Noise in reconstructed Stokes image s_1 (b) Denoising accuracy with burst imaging

(c) Averaged quantatitve results of Stokes vector components

Figure 5. **Noise in Stokes images and intensity denoising.** (a) Stokes vector s_1 reconstructed from a single-shot, single-shot with a learned intensity denoiser [66], and burst imaging (Pseudo GT) averaged over 100 shots. (b) Reconstruction accuracy of a Stokes image with varying number of averaged images. (c) Reconstruction accuracy of Stokes elements with and without intensity denoising.

5. Dataset Analysis

We provide our analysis of the acquired Stokes datasets.

Noise and Intensity Denoising Spectro-polarimetric images are susceptible to noise due to the low-light throughput of spectral and polarimetric filters. Our datasets are not exempt from these issues. To assess noise in Stokes images, we capture and average 100 images of a scene shown in Figure 3(c) for each polarization configuration Θ. From these averaged images, we reconstruct pseudo ground-truth Stokes image, shown in Figure 5(a). Figure 5(b) reports the MSE and PSNR of reconstructed Stokes images with respect to the number of averaged images. To achieve a PSNR exceeding 35 dB, we need to average over 4/25 shots for the trichromatic/hyperspectral Stokes cameras, indicating lower SNR of the hyperspectral Stokes dataset. We find that state-of-the-art learning-based intensity denoising methods, such as KBNet [66], can effectively reduce noise for each polarization configuration, leading to accurate Stokes-vector reconstruction, despite lack of polarization images during training. For the denoised single-shot capture, we achieve a PSNR of 34.5 dB, demonstrating the potential of using pretrained intensity restoration networks for Stokes imaging. Figure 5(c) shows PSNRs of reconstructed Stokes images per each spectral channel and Stokes element. With the intensity denoising, we find that the PSNR significantly increases for s_1, s_2, and s_3.

Efficient Spatio-spectral-polarimetric Representations Each pixel in a hyperspectral Stokes image contains a Stokes vector for every spectral channel, leading to a total

of $21 \times 4 \times 32$ bits using single-precision floating format. This results in a bit-per-pixel (BPP) value of 2,688, equating to 100 MB for storing a single hyperspectral Stokes image of 512×612 pixels. Given the substantial memory required to store a spectro-polarimetric image, we investigate efficient representations of real-world spatio-spectral-polarimetric data, for which we explore two methods: a PCA-based model and implicit neural model.

First, we conduct PCA on non-overlapping hyperspectral Stokes patches. Figure 4(a) shows the 40 most significant PCA bases, revealing varied spatial and spectral features for each Stokes element: s_0, s_1, s_2, s_3. Notably, spatial structures are more evident in s_0, while s_1, s_2, s_3 shows spectral features, suggesting a stronger correlation between spectrum and polarization than spatial features. To visualize hyperspectral intensity, we convert it to sRGB, which means that the same sRGB color may originate from different spectra. Figure 4(c) shows the variance of the coefficients for the top 200 PCA bases, indicating that spatio-spectral-polarimetric data can indeed be compressed. This is further evidenced by Figure 4(d), which shows the reconstruction error and BPP when varying number of PCA bases used to recreate a hyperspectral Stokes image. Using 2.22 MB coefficients adequately represents a 100 MB hyperspectral Stokes image as shown in Figure 4(b), exhibiting a high compression rate with the reconstruction error of 2.69×10^{-5}. See the Supplemental Document for further details on PCA analysis.

Second, we devise an INR for hyperspectral Stokes images by modifying the recently-proposed network architecture, NeSpoF [34]. The original NeSpoF architecture models a volumetric hyperspectral Stokes field. Here, instead, we aim to represent a hyperspectral Stokes image. Specifically, our INR, modeled by an MLP F_γ, outputs the Stokes vector $\mathbf{s}$ for a given pixel position p_x, p_y and spectral channel index c, that is

$$\mathbf{s} = F_\gamma(p_x, p_y, c), \tag{5}$$

where γ is the network parameters. We fit the MLP to a hyperspectral Stokes image by minimizing the reconstruction loss between the network output and the hyperspectral Stokes image. The training curve is shown in Figure 4(e). Figure 4(f) shows the reconstruction error and BPP of our INR with respect to varying number of the MLP layers. With just 8 layers corresponding to a BPP of 60, we achieve a converged reconstruction error of 1.90×10^{-5}, resulting in just 2.22 MB of network parameters to represent a 100 MB hyperspectral Stokes image. See Supplemental Document for architecture details.

Both PCA and INR experiments validate that a natural spectro-polarimetric image is compressible. PCA provides PCA basis vectors that can be applied to any instance, however with a lower reconstruction accuracy than INR.

(a) Separation into polarized and unpolarized light

(b) Intensity distribution by polarization

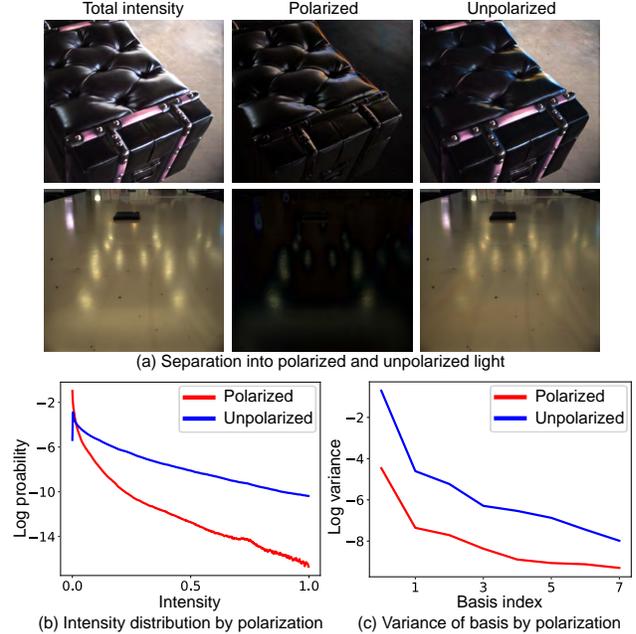(c) Variance of basis by polarization

Figure 6. **Polarized and unpolarized light distributions.** (a) Separation into polarized and unpolarized light. (b) Intensity distributions for polarized and unpolarized components. (c) Variance of PCA basis of polarized and unpolarized intensity across spectral channel.

INR is overfitted to a single instance, while higher reconstruction accuracy can be achieved. These representations are also beneficial for denoising spectral-polarimetric images, as shown in Figure 4(b), which even outperforms the learning-based intensity denoiser [66].

Polarized and Unpolarized Intensity We decompose hyperspectral Stokes images into the polarized images $P = \sqrt{s_1^2 + s_2^2 + s_3^2}$ and unpolarized images $U = s_0 - P$ per each spectral channel. Figure 6(a) shows specular reflections such as the glow of leather sofa separated into polarized light. Note that the polarized image typically encodes the illumination colors for dielectric surfaces. Figure 6(b) reveals that the intensity distributions of polarized light, obtained from the entire hyperspectral Stokes dataset, is skewed towards low and high-intensity values compared to the unpolarized light. This is because polarized images mostly contain specular reflections, which is sparsely distributed and has high intensity values. We then compute the variance of the PCA bases for polarized intensity along the spectral channel. Figure 6(c) highlights that the spectral variance for polarized intensity is lower than that of unpolarized intensity. We speculate that the color of polarized light lies in a lower dimensional space than that of unpolarized light, since diffuse reflection with diverse spectral variations is mostly captured by unpolarized light, making the spectral variation of unpolarized light more pronounced.
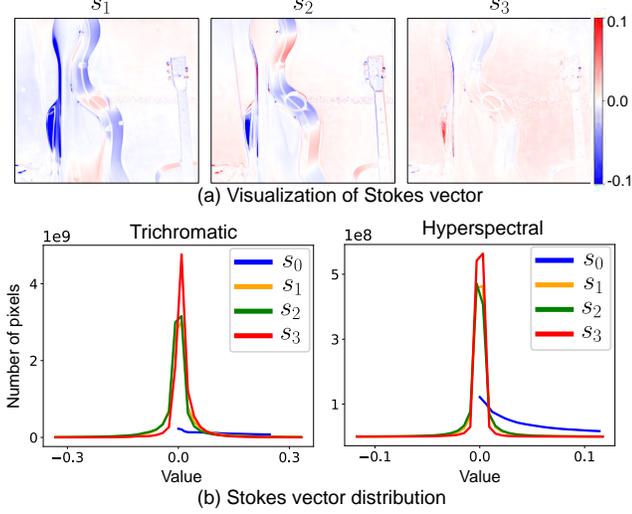
(a) Visualization of Stokes vector

(b) Stokes vector distribution

Figure 7. **Stokes-vector distributions.** (a) Stokes images of s_1, s_2, and s_3 at the green channel. (b) Stokes-vector distributions of s_0, s_1, s_2 and s_3 for trichromatic and hyperspectral datasets.

Stokes Vector Distributions in Natural Stokes Images
Next, we analyze the distribution of all Stokes vectors in our Stokes dataset. Figure 7 reports the histograms of Stokes elements s_0, s_1, s_2, s_3 across all spectral channel. We find that the distributions of Stokes elements (s_1, s_2, s_3) have symmetric shapes of positive and negative sides. Stokes elements of s_1 and s_2 have similar shapes meaning that the directions of linearly-polarized light are equally distributed in natural images. The circular component s_3 is more condensed near zero than the linear elements, resulting in a higher peak both in trichromatic and hyperspectral datasets. This indicates that pixels are often more linearly polarized than circularly polarized. Refer to the Supplemental Document for further analysis.

Gradient Analysis of Stokes Images Gradient distribution of images has been often used as priors for image-based applications including image restoration, understanding, and editing. Here, we perform gradient analysis of Stokes and polarization-feature images. Figure 8(b) shows that the gradient of Stokes and normalized Stokes vectors exhibits a similarity to Hyper-Laplacian priors, commonly used to describe the gradient of natural intensity-images. An interesting finding is that total intensity s_0 has more high-gradient values than the linear components of s_1 and s_2, and the circular component s_3 has the lowest-value distribution.

We then analyze the gradient distributions of polarization features, including AoLP, degree of linear polarization (DoLP), degree of circular polarization (DoCP), and CoP. DoLP and DoCP are computed as $\mathrm{DoLP} = \sqrt{s_1^2 + s_2^2}/s_0$ and $\mathrm{DoCP} = |s_3|/s_0$ respectively. To compute the gradient of AoLP images, we consider the angular wrapping

(a) Visualization of polarization features and gradients

(b) Gradient distributions of Stokes vector
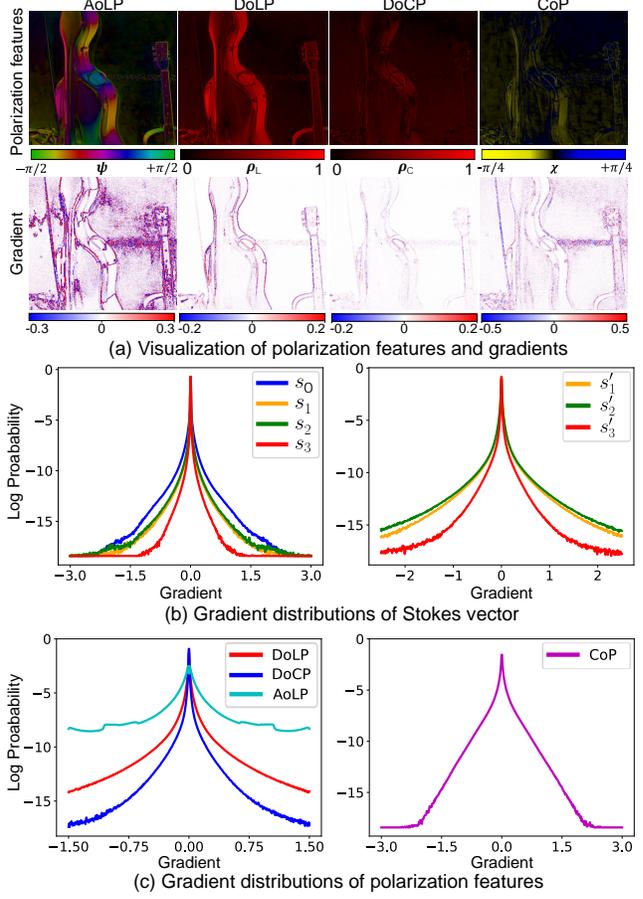
(c) Gradient distributions of polarization features

Figure 8. **Gradient analysis of Stokes images.** (a) Visualization of AoLP, DoLP, DoCP and CoP values and their gradients. Examining the log probability of the gradient for (b) Stokes vectors s_0, s_1, s_2, s_3 and normalized Stokes vectors s_1', s_2', and s_3', and (c) polarization features including DoLP, DoCP, AoLP and CoP.

property. That is, AoLP has a range from $-\frac{\pi}{2}$ to $\frac{\pi}{2}$ and the AoLPs of $-\frac{\pi}{2}$ and $\frac{\pi}{2}$ are identical. Thus, if the gradient exceeds $\frac{\pi}{2}$, we estimate the gradient as $\nabla\mathrm{AoLP} - \pi \times \mathrm{sign}(\nabla\mathrm{AoLP})$, where ∇ is the gradient operator and `sign` is the sign operator that returns 1 if positive, otherwise -1. Figure 8(c) shows that the gradients of AoLP are generally higher than DoLP and DoCP. This implies that sparsity in the measurement gradient is milder for AoLP than DoLP and DoCP. DoLP and DoCP have shapes similar to Hyper-Laplacian priors while DoCP is sharper than DoLP. The gradient of CoP shows symmetric distributions for right-circular and left-circular directions. Unlike AoLP, the probability decreases as the gradient approaches extreme values. The difference in tendency between linear-polarization and circular-polarization features, as well as their distributions, means that we need distinct priors for each polarization feature, emphasizing the importance of a full Stokes dataset that measure not only linear but also circular polarization.

(a) Trichromatic Stokes image   (b) Normal map from R channel   (c) Normal map from G channel   (d) Normal map from B channel

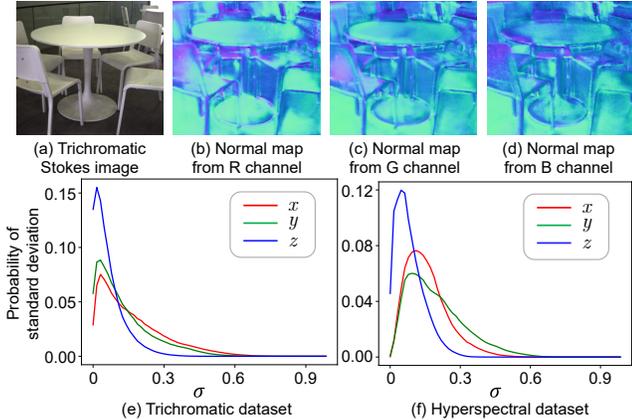(e) Trichromatic dataset   (f) Hyperspectral dataset

Figure 9. **Spectral dependency of conventional SFP method.** (a) Trichromatic Stokes image and estimated surface normals [41] for each red, green, and blue spectral channels shown in (b), (c), and (d). Graphs (e) and (f) show the probability distributions of standard deviation of normal component x, y, and z along the spectral channels for both datasets.

Shape from Polarization and Spectral Channels Methods that recover shape from polarization, SfP, have made rapid progress in the last decade. SfP aims to extract normals by analyzing the normal-dependent polarization change of reflected light. Specifically, SfP analyzes the DoP and AoLP based on Fresnel theory [9], which describes the polarization change of light upon reflection and transmission at a smooth surface [32, 41]. Here, we analyze an overlooked problem in SfP: the spectral dependency of estimated normals. Surface normals, as a geometric surface property, should be consistent regardless of the input spectral channels used for SfP. In Figure 9, we test the state-of-the-art SfP method by Lei et al. [41], designed for in-the-wild scenes. The evaluation results on our Stokes dataset clearly reveal that normal maps reconstructed from different spectral channels exhibit variations. We compute the standard deviations of spectral variations for each x, y, and z component of the estimated normals. Figures 9(e) and (f) show the probability distributions of the standard deviation, highlighting the large variations in the estimated normals for both hyperspectral and trichromatic datasets. Interestingly, the x and y components of normals show larger standard deviations than the z component. This implies that the spectral variation of DoP, which determines the z component, has less impact on the distribution than that of AoLP, which governs the x and y components. Our analysis underscores the development of a spectrum-aware SfP method as an interesting future research.

Environment Dependency Figure 10 shows the Poincaré spheres projected onto the $s_1' - s_2'$ and $s_1' - s_3'$ planes for the three data labels: *Indoor*, *Sunlight* and *Cloudy*. Sunlight is known to contain more circularly polarized light compared
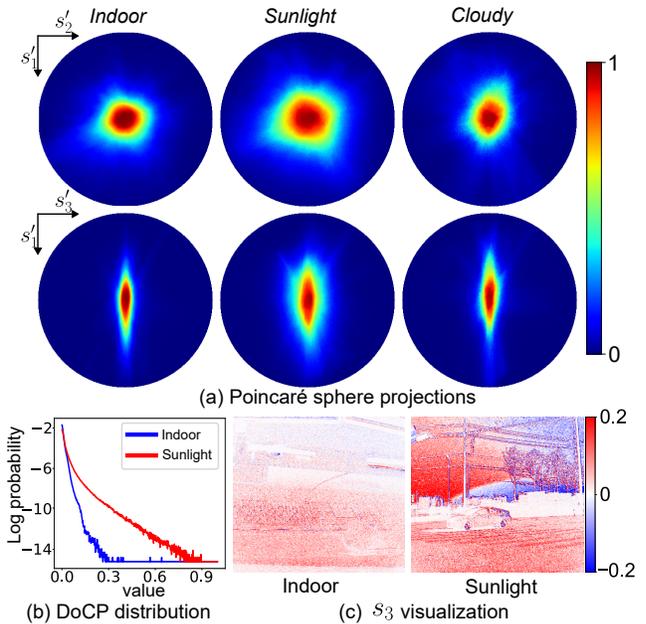

(a) Poincaré sphere projections

(b) DoCP distribution   (c) s_3 visualization

Figure 10. **Environment dependency.** (a) Projected Poincaré spheres onto the $s_1' - s_2'$ and $s_1' - s_3'$ planes with repsect to dataset labels. Colorbar is based on the normalized pixel count. (b) DoCP distributions for indoor and sunlight cateogries. (c) Example s_3 images.

to other artificial lighting [25]. As shown in Figure 10(a), Stokes vectors are distributed more widely across s_3' axis under sunlight compared with Indoor scene. In addition, we find that DoCP is distributed at higher values for the sunlight compared to the indoor: pixels with DoCP over 0.5 are rarely observed in indoor scenes. This is also confirmed in the example s_3 images for indoor and sunlight scenes.

Another interesting finding is that cloudy or sunny illumination result in different polarization statistics. Figure 10(a) shows that Stokes vectors of cloudy scenes are more concentrated near the origin, meaing that light is more depolarized compared to light under clear sunlight. This is aligned with previous studies [24, 58] that report the impact of cloud-particle scatterings on light depolarization.

6. Conclusion

In this work, we have introduced a novel trichromatic and hyperspectral Stokes image dataset that encompasses diverse natural scenes and various illumination conditions, totaling more than 2,333 scenes. We analyze the empirical distribution of the Stokes vectors of natural spectro-polarimetric images. To efficiently represent spatio-spectral-polarimetric data, we devise a PCA-based model and an implicit neural representation. We further provide detailed analysis on Stokes gradient distributions, denoising characteristics, spectral dependency of SfP, and environment dependency. As such, our work provides a foun-

dation for future research on spectral-polarimetric imaging and vision.

References

[1] Jean-Baptiste Alayrac, Jeff Donahue, Pauline Luc, Antoine Miech, Iain Barr, Yana Hasson, Karel Lenc, Arthur Mensch, Katie Millican, Malcolm Reynolds, Roman Ring, Eliza Rutherford, Serkan Cabi, Tengda Han, Zhitao Gong, Sina Samangooei, Marianne Monteiro, Jacob Menick, Sebastian Borgeaud, Andrew Brock, Aida Nematzadeh, Sahand Sharifzadeh, Mikolaj Binkowski, Ricardo Barreira, Oriol Vinyals, Andrew Zisserman, and Karen Simonyan. Flamingo: a visual language model for few-shot learning, 2022. 1

[2] Eleni Aloupogianni, Takaya Ichimura, Mei Hamada, Masahiro Ishikawa, Takuo Murakami, Atsushi Sasaki, Koichiro Nakamura, Naoki Kobayashi, and Takashi Obi. Hyperspectral imaging for tumor segmentation on pigmented skin lesions. *Journal of Biomedical Optics*, 27(10):106007, 2022. 1

[3] Ali Altaqui, Pratik Sen, Harry Schrickx, Jeromy Rech, Jin-Woo Lee, Michael Escuti, Wei You, Bumjoon J Kim, Robert Kolbas, Brendan T O'Connor, et al. Mantis shrimp–inspired organic photodetector for simultaneous hyperspectral and polarimetric imaging. *Science Advances*, 7(10):eabe3196, 2021. 1

[4] Yunhao Ba, R. Chen, Yiqin Wang, Lei Yan, Boxin Shi, and Achuta Kadambi. Physics-based neural networks for shape from polarization. *ArXiv*, abs/1903.10210, 2019. 1, 2

[5] Yunhao Ba, Alex Gilbert, Franklin Wang, Jinfa Yang, Rui Chen, Yiqin Wang, Lei Yan, Boxin Shi, and Achuta Kadambi. Deep shape from polarization. In *Eur. Conf. Comput. Vis.*, pages 554–571. Springer, 2020. 2, 3

[6] Seung-Hwan Baek and Felix Heide. Polarimetric spatio-temporal light transport probing. *ACM Trans. Graph.*, 40(6):1–18, 2021. 2

[7] Seung-Hwan Baek, Daniel S Jeon, Xin Tong, and Min H Kim. Simultaneous acquisition of polarimetric svbrdf and normals. *ACM Trans. Graph.*, 37(6):268–1, 2018. 1, 2

[8] Michael Baltaxe, Tomer Pe'er, and Dan Levi. Polarimetric imaging for perception, 2023. 1

[9] Edward Collett. Field guide to polarization. Spie Bellingham, WA, 2005. 1, 3, 4, 8

[10] Qi Cui, Jongchan Park, Yayao Ma, and Liang Gao. Snapshot hyperspectral light field tomography. *Optica*, 8(12):1552–1558, 2021. 1

[11] Akshat Dave, Yongyi Zhao, and Ashok Veeraraghavan. Pandora: Polarization-aided neural decomposition of radiance. *arXiv preprint arXiv:2203.13458*, 2022. 1, 2, 3

[12] Fernando del Molino and Adolfo Muñoz. Polarization mapping. *Computers & Graphics*, 83:42–50, 2019. 2

[13] Louis J Denes, Milton S Gottlieb, Boris Kaminsky, and Daniel F Huber. Spectropolarimetric imaging for object recognition. In *26th AIPR Workshop: Exploiting New Image Sources and Sensors*, volume 3240, pages 8–18. SPIE, 1998. 1, 2

[14] Jia Deng, Wei Dong, Richard Socher, Li-Jia Li, Kai Li, and Li Fei-Fei. Imagenet: A large-scale hierarchical image database. In *IEEE Conf. Comput. Vis. Pattern Recog.*, pages 248–255, 2009. 1

[15] Valentin Deschaintre, Yiming Lin, and Abhijeet Ghosh. Deep polarization imaging for 3d shape and svbrdf acquisition. In *IEEE Conf. Comput. Vis. Pattern Recog.*, pages 15567–15576, 2021. 2

[16] Yuqi Ding, Yu Ji, Mingyuan Zhou, Sing Bing Kang, and Jinwei Ye. Polarimetric helmholtz stereopsis. In *Int. Conf. Comput. Vis.*, pages 5037–5046, 2021. 2

[17] Axin Fan, Tingfa Xu, Xu Ma, Jianan Li, Xi Wang, Yuhan Zhang, and Chang Xu. Four-dimensional compressed spectropolarimetric imaging. *Signal Processing*, 2022. 1

[18] Axin Fan, Tingfa Xu, Geer Teng, Xi Wang, Yuhan Zhang, and Chenguang Pan. Hyperspectral polarization-compressed imaging and reconstruction with sparse basis optimized by particle swarm optimization. *Chemometrics and Intelligent Laboratory Systems*, 206:104163, 2020. 1

[19] Axin Fan, Tingfa Xu, Geer Teng, Wang Xi, Yuhan Zhang, Chang Xu, Xin Xu, and Jianan Li. Full-stokes polarization multispectral images of various stereoscopic objects. *Scientific Data*, 10, 05 2023. 1, 2, 3

[20] Shuai Fang, XiuShan Xia, Xing Huo, and ChangWen Chen. Image dehazing using polarization effects of objects and airlight. *Opt. Express*, 22(16):19523–19537, Aug 2014. 2

[21] Yoshiki Fukao, Ryo Kawahara, Shohei Nobuhara, and Ko Nishino. Polarimetric normal stereo. In *Int. Conf. Comput. Vis.*, pages 682–690, 2021. 2

[22] Daoyi Gao, Yitong Li, Patrick Ruhkamp, Iuliia Skobleva, Magdalena Wysocki, HyunJun Jung, Pengyuan Wang, Arturo Guridi, and Benjamin Busam. Polarimetric pose prediction. In *Eur. Conf. Comput. Vis.*, October 2022. 1, 3

[23] Missael Garcia, Christopher Edmiston, Radoslav Marinov, Alexander Vail, and Viktor Gruev. Bio-inspired color-polarization imager for real-time in situ imaging. *Optica*, 4(10):1263–1271, 2017. 1

[24] Ramón Hegedüs, Susanne Åkesson, and Gábor Horváth. Polarization patterns of thick clouds: overcast skies have distribution of the angle of polarization similar to that of clear skies. *J. Opt. Soc. Am. A*, 24(8):2347–2356, Aug 2007. 8

[25] Gábor Horváth and Dezsö Varjú. *Polarized light in animal vision: polarization patterns in nature*. Springer Science & Business Media, 2004. 1, 8

[26] Daniel F Huber, Louis Denes, Martial Hebert, Milton Gottlieb, Boris Kaminsky, and Peter Metes. A spectro-polarimetric imager for intelligent transportation systems. 1997. 1

[27] Cong Phuoc Huynh, Antonio Robles-Kelly, and Edwin R Hancock. Shape and refractive index from single-view spectro-polarimetric images. *Int. J. Comput. Vis.*, 101(1):64–94, 2013. 1

[28] Nevrez Imamoglu, Yu Oishi, Xiaoqiang Zhang, Guanqun Ding, Yuming Fang, Toru Kouyama, and Ryosuke Nakamura. Hyperspectral image dataset for benchmarking on salient object detection. In *2018 Tenth international conference on quality of multimedia experience (qoMEX)*, pages 1–3. IEEE, 2018. 1

[29] Md Nazrul Islam, Murat Tahtali, and Mark Pickering. Specular reflection detection and inpainting in transparent object through msplfi. *IEEE Transactions on Geoscience and Re-*

mote Sensing. 2

[30] Md Nazrul Islam, Murat Tahtali, and Mark Pickering. Hybrid fusion-based background segmentation in multispectral polarimetric imagery. *IEEE Transactions on Geoscience and Remote Sensing*, 12(11):1776, 2020. 1, 2

[31] Achuta Kadambi, Vage Taamazyan, Boxin Shi, and Ramesh Raskar. Polarized 3d: High-quality depth sensing with polarization cues. In *Int. Conf. Comput. Vis.*, pages 3370–3378, 2015. 2

[32] Achuta Kadambi, Vage Taamazyan, Boxin Shi, and Ramesh Raskar. Depth sensing using geometrically constrained polarization normals. *Int. J. Comput. Vis.*, 125(1):34–51, 2017. 8

[33] Agastya Kalra, Vage Taamazyan, Supreeth Krishna Rao, Kartik Venkataraman, Ramesh Raskar, and Achuta Kadambi. Deep polarization cues for transparent object segmentation. In *IEEE Conf. Comput. Vis. Pattern Recog.*, June 2020. 2

[34] Youngchan Kim, Wonjoon Jin, Sunghyun Cho, and Seung-Hwan Baek. Neural spectro-polarimetric fields. *arXiv preprint arXiv:2306.12562*, 2023. 3, 4, 6

[35] Alexander Kirillov, Eric Mintun, Nikhila Ravi, Hanzi Mao, Chloe Rolland, Laura Gustafson, Tete Xiao, Spencer Whitehead, Alexander C. Berg, Wan-Yen Lo, Piotr Dollár, and Ross Girshick. Segment anything. *arXiv:2304.02643*, 2023. 1

[36] Yuhi Kondo, Taishi Ono, Legong Sun, Yasutaka Hirasawa, and Jun Murayama. Accurate polarimetric brdf for real polarization scene rendering. In *Eur. Conf. Comput. Vis.*, pages 220–236. Springer, 2020. 1, 2, 3

[37] Naejin Kong, Yu-Wing Tai, and Joseph S. Shin. A physically-based approach to reflection separation: From physical modeling to constrained optimization. *IEEE Transactions on Pattern Analysis and Machine Intelligence*, 36(2):209–221, 2014. 2

[38] Teppei Kurita, Yuhi Kondo, Legong Sun, and Yusuke Moriuchi. Simultaneous acquisition of high quality rgb image and polarization. In *Proceedings of the IEEE/CVF Winter Conference on Applications of Computer Vision (WACV)*, pages 178–188, January 2023. 1, 3

[39] Pierre-Jean Lapray, Luc Gendre, Alban Foulonneau, and Laurent Bigué. Database of polarimetric and multispectral images in the visible and nir regions. 04 2018. 1, 2, 3

[40] Chenyang Lei, Xuhua Huang, Mengdi Zhang, Qiong Yan, Wenxiu Sun, and Qifeng Chen. Polarized reflection removal with perfect alignment in the wild. In *IEEE Conf. Comput. Vis. Pattern Recog.*, June 2020. 1, 2, 3

[41] Chenyang Lei, Chenyang Qi, Jiaxin Xie, Na Fan, Vladlen Koltun, and Qifeng Chen. Shape from polarization for complex scenes in the wild. In *IEEE Conf. Comput. Vis. Pattern Recog.*, pages 12632–12641, June 2022. 2, 3, 8

[42] Yupeng Liang, Ryosuke Wakaki, Shohei Nobuhara, and Ko Nishino. Multimodal material segmentation. In *IEEE Conf. Comput. Vis. Pattern Recog.*, pages 19800–19808, June 2022. 1, 2, 3

[43] Fei Liu, Lei Cao, Xiaopeng Shao, Pingli Han, and Xiangli Bin. Polarimetric dehazing utilizing spatial frequency segregation of images. *Applied Optics*, 54(27):8116–8122, 2015. 2

[44] Ming Liu, Zhongqiu Sun, Shan Lu, and Kenji Omasa. Combining multiangular, polarimetric, and hyperspectral measurements to estimate leaf nitrogen concentration from different plant species. *IEEE Transactions on Geoscience and Remote Sensing*, 60:1–15, 2021. 2

[45] Xiaobo Lv, Yiwei Li, Shuaishuai Zhu, Xinmin Guo, Jianlong Zhang, Jie Lin, and Peng Jin. Snapshot spectral polarimetric light field imaging using a single detector. *Optics Letters*, 45(23):6522–6525, 2020. 1

[46] Youwei Lyu, Zhaopeng Cui, Si Li, Marc Pollefeys, and Boxin Shi. Reflection separation using a pair of unpolarized and polarized images. In H. Wallach, H. Larochelle, A. Beygelzimer, F. d'Alché-Buc, E. Fox, and R. Garnett, editors, *Adv. Neural Inform. Process. Syst.*, volume 32. Curran Associates, Inc., 2019. 1, 2, 3

[47] Alkhazur Manakov, John Restrepo, Oliver Klehm, Ramon Hegedus, Elmar Eisemann, Hans-Peter Seidel, and Ivo Ihrke. A reconfigurable camera add-on for high dynamic range, multispectral, polarization, and light-field imaging. *ACM Trans. Graph.*, 32(4):47–1, 2013. 1

[48] Haiyang Mei, Bo Dong, Wen Dong, Jiaxi Yang, Seung-Hwan Baek, Felix Heide, Pieter Peers, Xiaopeng Wei, and Xin Yang. Glass segmentation using intensity and spectral polarization cues. In *IEEE Conf. Comput. Vis. Pattern Recog.*, pages 12622–12631, 2022. 1, 2, 3

[49] Tingkui Mu, Donghao Bao, Feng Han, Yuanyuan Sun, Zeyu Chen, Qian Tang, and Chunmin Zhang. Optimized design, calibration, and validation of an achromatic snapshot full-stokes imaging polarimeter. *Optics Express*, 27(16):23009–23028, 2019. 1

[50] Tingkui Mu, Shaun Pacheco, Zeyu Chen, Chunmin Zhang, and Rongguang Liang. Snapshot linear-stokes imaging spectropolarimeter using division-of-focal-plane polarimetry and integral field spectroscopy. *Scientific reports*, 7(1):42115, 2017. 1

[51] Shree K Nayar, Xi-Sheng Fang, and Terrance Boult. Separation of reflection components using color and polarization. *Int. J. Comput. Vis.*, 21(3):163–186, 1997. 2

[52] Simeng Qiu, Qiang Fu, Congli Wang, and Wolfgang Heidrich. Linear polarization demosaicking for monochrome and colour polarization focal plane arrays. *Comput. Graph. Forum*, 40, 03 2021. 1, 2, 3

[53] Aditya Ramesh, Mikhail Pavlov, Gabriel Goh, Scott Gray, Chelsea Voss, Alec Radford, Mark Chen, and Ilya Sutskever. Zero-shot text-to-image generation, 2021. 1

[54] Shuhei Shibata, Nathan Hagen, and Yukitoshi Otani. Robust full stokes imaging polarimeter with dynamic calibration. *Optics letters*, 44(4):891–894, 2019. 1

[55] Canran Tu, Peng Li, Zhenhong Li, Houjie Wang, Shuowen Yin, Dahui Li, Quantao Zhu, Maoxiang Chang, Jie Liu, and Guoyang Wang. Synergetic classification of coastal wetlands over the yellow river delta with gf-3 full-polarization sar and zhuhai-1 ohs hyperspectral remote sensing. *IEEE Transactions on Geoscience and Remote Sensing*, 13(21):4444, 2021. 1, 2

[56] Xingzhou Tu, Scott McEldowney, Yang Zou, Matthew Smith, Christopher Guido, Neal Brock, Sawyer Miller, Linan Jiang, and Stanley Pau. Division of focal plane red–green–blue full-stokes imaging polarimeter. *Appl. Opt.*,

59(22):G33–G40, Aug 2020. 3

[57] Xingzhou Tu, Oliver J Spires, Xiaobo Tian, Neal Brock, Rongguang Liang, and Stanley Pau. Division of amplitude rgb full-stokes camera using micro-polarizer arrays. *Optics Express*, 25(26):33160–33175, 2017. 4

[58] John D. van der Laan, Jeremy B. Wright, David A. Scrymgeour, Shanalyn A. Kemme, and Eustace L. Dereniak. Evolution of circular and linear polarization in scattering environments. *Opt. Express*, 23(25):31874–31888, Dec 2015. 8

[59] Sijia Wen, Yinqiang Zheng, and Feng Lu. Polarization guided specular reflection separation. *IEEE Trans. Image Process.*, 30:7280–7291, 2021. 2

[60] Alexander Wilkie and Andrea Weidlich. A standardised polarisation visualisation for images. In *Proceedings of the 26th Spring Conference on Computer Graphics*, pages 43–50, 2010. 3

[61] Pu Xia and Xuebin Liu. Image dehazing technique based on polarimetric spectral analysis. *Optik*, 127(18):7350–7358, 2016. 2

[62] Fanchao Yang, Xingjia Tang, Bingliang Hu, Ruyi Wei, Liang Kong, and Yong Li. A method of removing reflected highlight on images based on polarimetric imaging. *Journal of Sensors*, 2016, 2016. 2

[63] Hang Yao, Bolin Fu, Ya Zhang, Sunzhe Li, Shuyu Xie, Jiaoling Qin, Donglin Fan, and Ertao Gao. Combination of hyperspectral and quad-polarization sar images to classify marsh vegetation using stacking ensemble learning algorithm. *IEEE Transactions on Geoscience and Remote Sensing*, 14(21):5478, 2022. 1, 2

[64] Lu Yuan, Dongdong Chen, Yi-Ling Chen, Noel Codella, Xiyang Dai, Jianfeng Gao, Houdong Hu, Xuedong Huang, Boxin Li, Chunyuan Li, Ce Liu, Mengchen Liu, Zicheng Liu, Yumao Lu, Yu Shi, Lijuan Wang, Jianfeng Wang, Bin Xiao, Zhen Xiao, Jianwei Yang, Michael Zeng, Luowei Zhou, and Pengchuan Zhang. Florence: A new foundation model for computer vision, 2021. 1

[65] Junping Zhang, Jian Tan, and Ye Zhang. Joint sparse tensor representation for the target detection of polarized hyperspectral images. *IEEE Transactions on Geoscience and Remote Sensing*, 14(12):2235–2239, 2017. 2

[66] Yi Zhang, Dasong Li, Xiaoyu Shi, Dailan He, Kangning Song, Xiaogang Wang, Hongwei Qin, and Hongsheng Li. Kbnet: Kernel basis network for image restoration, 2023. 5, 6

[67] Yongqiang Zhao, Lei Zhang, and Quan Pan. Spectropolarimetric imaging for pathological analysis of skin. *Applied optics*, 48(10):D236–D246, 2009. 1, 2

[68] Chu Zhou, Minggui Teng, Yufei Han, Chao Xu, and Boxin Shi. Learning to dehaze with polarization. *Adv. Neural Inform. Process. Syst.*, 34:11487–11500, 2021. 2

[69] Chu Zhou, Minggui Teng, Youwei Lyu, Si Li, Chao Xu, and Boxin Shi. Polarization-aware low-light image enhancement. In *Proc. of the AAAI Conference on Artificial Intelligence*, pages 3742–3750, 2023. 2

[70] Shihao Zou, Xinxin Zuo, Yiming Qian, Sen Wang, Chi Xu, Minglun Gong, and Li Cheng. 3d human shape reconstruction from a polarization image. In *Eur. Conf. Comput. Vis.*, pages 351–368. Springer, 2020. 2